Amesia
https://dergipark.org.tr/en/pub/amesia
Open Access

e-ISSN: 3108-3579 6 (2) (2025) 90-112 doi.org/10.54559/amesia.1755059

Two-Dimensional Numerical Study of Mixed Convection Evaporation from an Inclined Wet Corrugated Plate

Ando Pascal Dimbiharizafy[1], Ignace Andrianarivo Rakotozandry[2], Josoa Albert Randriamorasata[3]

Article Info
Received: 31 Jul 2025
Accepted: 13 Oct 2025
Published: 31 Dec 2025
Research Article

Abstract − This paper presents the two-dimensional numerical study of mixed convection evaporation from an inclined corrugated wet plate subjected to a constant heat flux density. Assumptions were adopted and boundary conditions are imposed so as to neglect certain terms in the continuity, momentum, heat and diffusion equations that govern the phenomenon on the boundary layers. The homotopic transformation then allows the equation of the curve to be transformed from a corrugation to that of a straight line. Adimensionnalization allowed us not only to link physical parameters together but also to obtain equations that no longer depend on the measurement systems. From the dimensionless equations, we were able to apply the implicit finite difference method. The numerical resolution of the obtained discretized equations was programmed on MATLAB. We have examined and presented the influences of wavelength, wave amplitude, and plate inclination on the dimensionless velocity, temperature, and concentration fields, as well as on the corresponding friction coefficient, Nusselt number, and Sherwood number. Depending on the dimensionless quantity or the exchange coefficient studied, the effects of the inclination of the plate, the wavelength and the wave amplitude can be similar, or two variables cause the same effect, but the third variable generates the opposite effect. Results for unstable numerical schemes on the dimensionless velocity distribution were obtained when we increased the value of the Reynolds number, the x-step, the y-step or when we decreased the value of the Richardson number indicating that the supposed laminar flow tends towards a turbulent regime.

Keywords − *Adimensionalization, boundary layer, homotopic transformation, implicit finite difference method, Nusselt number*

1. Introduction

Flows on a wall have interested many researchers through industrial applications such as the cooling of nuclear reactors [1, 2] and the drying of food [3]. Most of the studies concerned a simple geometry such as a flat plate [4-6] or an inclined tube [7]. However, industrial reality is moving towards more complex configurations, and the geometric shape influences the performance of a thermal system [8]. Work has been carried out on corrugated plates, and the parameters studied differ from each study, such as the influences of the wave amplitude and pressure losses or the formation of recirculation zones [9, 10]. The coupled transfers of heat and mass on an inclined corrugated plate have been just touched upon by previous research. Some researchers have opted for forced flows only or natural flows only [11-13]. Studying the effects of undulation and those of the inclination of a plate at the same time during evaporation by mixed convection thus has its interest. It will allow to delve into the heart of the phenomena involved and to complete the knowledge on these. In each study on mixed convection, there are neglected phenomena such as those of the wall laws or the assumption of a

[1]andodimbiharizafy@gmail.com (Corresponding Author); [2]ignacekool@yahoo.fr; [3]morasajoso@yahoo.fr
[1,2,3]Mechanical and Thermal Industrial Engineering, School of Engineering and Geosciences, University of Antananarivo, Antananarivo, Madagascar

Newtonian [14, 15] and incompressible fluid [16, 17]. It is the same for the geometric configuration in the presence of inclination and undulation. Studies concerned, for example, inclined solar exchangers [18], sinusoidal surfaces in vibration [19], half-spheres with undulated surface [20], and undulated enclosures [21].

The Latina letters, Greek letters, and dimensionless numbers used in the paper are provided in Table 1.

Table 1. Notations used in this paper

Latina Letters	i, j : Indices
$\vec{U}$: Velocity vector	f : Ondulation function
P : Driving pressure [Pa]	**Greek Letters**
$\overrightarrow{F_P}$: Volume force vector	ρ_0 : Air density at wall level [kg/m^3]
T_0 : Air temperature on the wall [K]	μ : Air dynamic viscosity [kg/ms]
C_0 : Air + water vapor concentration on the wall [mol/m^3]	ρ : Air density [kg/m^3]
a_T : Air thermal diffusivity [m²/s]	ϑ : Air kinematic viscosity [m²/s]
a_C : Air mass diffusivity [m²/s]	ζ : Load loss coefficient
T : Boundary layer temperature [K]	α : Plate inclination [rad]
C : Boundary layer concentration [mol/m^3]	λ : Air thermal conductivity [W/mK]
U_∞ : Air velocity on the entrance to the wall [m/s]	ε_T : Numerical scheme error
T_∞ : Air temperature on the entrance to the wall [K]	θ , χ : Dimensionless temperature and concentration
C_∞ : Air + water vapor concentration on the entrance to the wall [mol/m^3]	ξ, η : Homotopic coordinates
U, V : Components of dimensionless velocity	u_ξ, u_η : U components in R(0, $\overrightarrow{e_\xi}$,$\overrightarrow{e_\eta}$)
u_x , u_y : U components in R(O, $\vec{\imath}$, $\vec{\jmath}$)	$\overrightarrow{e_\xi}$, $\overrightarrow{e_\eta}$: units vectors in homotopic basis
$\vec{\imath}$, $\vec{\jmath}$: units vectors in Cartesian basis	β_T : Thermal expansion coefficient [K^{-1}]
Lv : Latente heat of water's vaporisation [J/Kg]	β_C : Volume expansion coefficient [m^{-3}]
X, Y : dimensionless variables	Δx, Δy: x-step and y-step
D : Air molecular diffusion [m²/s]	**Dimensionless numbers**
g : Gravity acceleration [m/s²]	Sh : Sherwood number
q : Heat flux density [W/m²]	Re : Reynolds number
C_{fx} : Friction coefficient	Pr : Prandlt number
L_0 : Wavelength [m]	Sc : Schmidt number
A_0 : Ondulation amplitude [m]	Ri : Richardson number
K : Metric coefficient of homotopic transformation	Nu : Nusselt number
$F_{i,j}$: Dimensionless quantity on i and j	Gr_T : Thermal Grashof number
L : Plate length [m]	Gr_C : Massic Grashof number

2. Problem Description

We consider a wet corrugated plate inclined at an angle α relative to the horizontal, of finite length L, subject to a constant heat flux density q and immersed in an ascending air flow assumed to be laminar, governed by the laws of natural and forced convection.

Air, considered as an ideal fluid, is characterized by a temperature T_∞, a velocity U_∞, and a concentration of air and water vapor C_∞ at the inlet of the heated part. For our study, we will consider only favorable mixed convection; in other words, the forced and natural flows occur in the same direction. The ripple is formed by periodic oscillations along the wall. It is U-shaped and is characterized by a wavelength L_O and a wave amplitude A_O. Figure 1 shows the characteristic diagram of our problem.

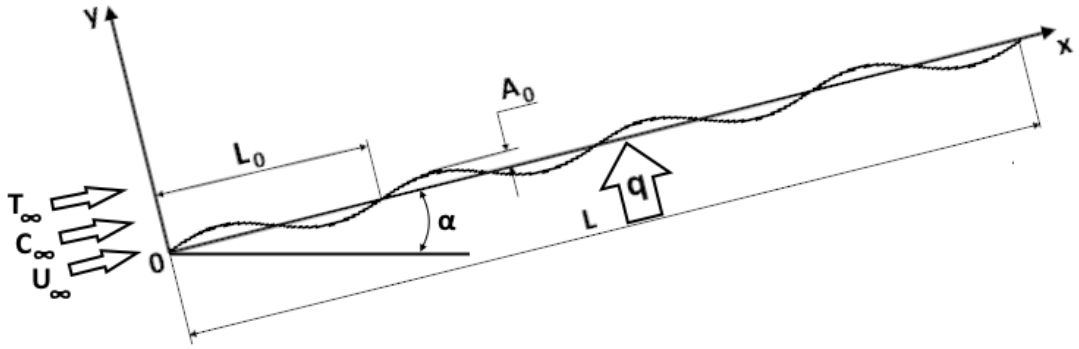

Figure 1. Characteristic scheme of the problem

2.1. Mathematical Formulation of the Problem

The equations of continuity, momentum, heat, and diffusion govern the phenomenon of evaporation by mixed convection. They are described by the system of (2.1) – (2.4).

$$\frac{\partial \rho}{\partial t} + \mathrm{div}\left(\rho \vec{U}\right) = 0 \tag{2.1}$$

$$\rho \frac{d\vec{U}}{dt} + \left(\vec{U}\mathrm{grad}\right)\vec{U} = -\overrightarrow{\mathrm{grad}}P + \mu \Delta U + \left(\zeta + \frac{\vartheta}{3}\right)\overrightarrow{\mathrm{grad}}\mathrm{div}\vec{U} + \rho\overrightarrow{F_P} \tag{2.2}$$

$$\frac{\partial T}{\partial t} + \left(\vec{U}.\overrightarrow{\mathrm{grad}}\right)T = a_T \nabla^2 T \tag{2.3}$$

$$\frac{\partial C}{\partial t} + \left(\vec{U}.\overrightarrow{\mathrm{grad}}\right)C = a_C \nabla^2 C \tag{2.4}$$

2.2. Choice and Consequences of Assumptions

For our study, we consider the following assumptions:

i. A two-dimensional, laminar, and steady flow,
ii. Uniform heat transfer and flow velocity,
iii. A Newtonian and incompressible fluid,
iv. The Soret and Dufour effects are neglected,
v. The application of the Boussinesq approximation.

The system of (2.1) – (2.4) becomes the system of (2.5) – (2.8).

$$\frac{\partial u_x}{\partial x} + \frac{\partial u_y}{\partial y} = 0 \tag{2.5}$$

$$u_x \frac{\partial u_x}{\partial x} + u_y \frac{\partial u_x}{\partial y} = g \sin\alpha\beta_T (T - T_\infty) \; - g \sin\alpha\beta_C (C - C_\infty) + \upsilon \frac{\partial^2 u_x}{\partial y^2} \tag{2.6}$$

$$u_x \frac{\partial T}{\partial x} + u_y \frac{\partial T}{\partial y} = a_T \frac{\partial^2 T}{\partial y^2} \tag{2.7}$$

$$u_x \frac{\partial C}{\partial x} + u_y \frac{\partial C}{\partial y} = a_C \frac{\partial^2 C}{\partial y^2} \tag{2.8}$$

Boundary conditions are given below. At the wall y=0, we have

$$\begin{aligned} u_x &= 0 \,, \\ q &= -\lambda \frac{\partial T}{\partial y}\Big|_{y=0} - \rho L v D \frac{\partial C}{\partial y}\Big|_{y=0} . \end{aligned} \tag{2.9}$$

Far from the wall y → ∞,

$$u_x \to u_\infty \,,$$

$$T \to T_\infty \,,$$

and

$$C \to T_\infty \,.$$

3. Methodology

3.1. Homotopic Transformation of the Equations

Consider a corrugated plate whose corrugation profile obeys (3.1).

$$y = A_0 \sin\frac{2\pi x}{L_0} \tag{3.1}$$

The homotopic method allows us to transform the curve described by a wave into the equation of a straight line. To do this, we introduce the homotopic transformations of (3.2):

$$\begin{cases} x = \xi \\ y = \eta \, f(\xi). \end{cases} \tag{3.2}$$

Here, $f(\xi) = A_0 \sin\frac{2\pi\xi}{L_0}$. For a vector quantity U, the homotopy invariance theorem allows us (3.3) [22].

$$u_x \vec{\imath} + u_y \vec{\jmath} = u_\xi \overrightarrow{e_\xi} + u_\eta \overrightarrow{e_\eta} \tag{3.3}$$

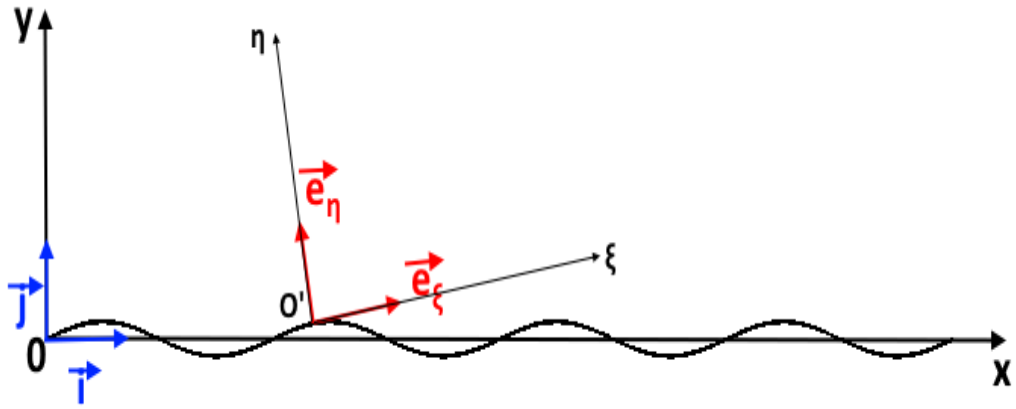

Figure 2. Change of reference frame from the Cartesian system to the homotopic system

In (3.3), we have the expressions for the terms of (3.4) – (3.6).

$$u_x = \frac{u_\xi}{K} \tag{3.4}$$

$$u_y = \frac{\eta f'(\xi)}{K} u_\xi + u_\eta \tag{3.5}$$

$$K = [1 + (\eta f'(\xi))^2]^{1/2} \tag{3.6}$$

(2.5) – (2.8) become (3.7) – (3.10), respectively.

$$\frac{\partial}{\partial \xi}\left(\frac{u_\xi}{K}\right) + \frac{f'(\xi)}{f(\xi)}\frac{u_\xi}{K} + \eta\frac{f'(\xi)}{f(\xi)}\frac{\partial}{\partial \eta}\left(\frac{u_\xi}{K}\right) + \frac{\partial}{\partial \eta}\left(\frac{u_\eta}{f(\xi)}\right) = 0 \tag{3.7}$$

$$\vartheta\frac{1}{f(\xi)^2}\frac{\partial^2}{\partial \eta^2}\left(\frac{u_\xi}{K}\right) - \left(\eta\frac{f'(\xi)}{f(\xi)}\frac{u_\xi}{K} + \frac{u_\eta}{f(\xi)}\right)\frac{\partial}{\partial \eta}\left(\frac{u_\xi}{K}\right) = \frac{u_\xi}{K}\frac{\partial}{\partial \xi}\left(\frac{u_\xi}{K}\right) - g\sin\alpha\beta_T(T - T_\infty) - g\sin\alpha\beta_C(C - C_\infty) \tag{3.8}$$

$$a_T\frac{1}{f(\xi)^2}\frac{\partial^2 T}{\partial \eta^2} + u_\eta\frac{1}{f(\xi)}\frac{\partial T}{\partial \eta} = -\frac{u_\xi}{K}\frac{\partial T}{\partial \xi} \tag{3.9}$$

$$a_C\frac{1}{f(\xi)^2}\frac{\partial^2 C}{\partial \eta^2} + u_\eta\frac{1}{f(\xi)}\frac{\partial C}{\partial \eta} = -\frac{u_\xi}{K}\frac{\partial C}{\partial \xi} \tag{3.10}$$

With boundary conditions are given below. At the wall $\eta = 0$:

$$u_\xi = 0\,,$$
$$T = T_0\,,$$

and

$$C = C_0\,.$$

Far from the wall $\eta \to \infty$:

$$u_\xi \to u_\infty\,,$$
$$T \to T_\infty\,,$$

and

$$C \to C_\infty\,.$$

3.2. Adimensionalization of Equations

Adimensionalization allows dimensionless quantities to appear in transfer equations. This method reduces the number of physical parameters in problems and allows for solutions that are no longer functions of measurement systems.

Introduce the following dimensionless variables and numbers:

$$X = \frac{\xi}{L}, \qquad Y = \frac{\eta f(\xi)}{L}, \qquad U = \frac{1}{K}\frac{u_\xi}{u_\infty}, \qquad V = \frac{1}{u_\infty}\left(\frac{\eta f'(\xi)}{K}u_\xi + u_\eta\right),$$

$$\theta = \frac{T - T_\infty}{T_0 - T_\infty}, \qquad \chi = \frac{C - C_\infty}{C_0 - C_\infty}, \qquad Re = \frac{u_\infty L}{\vartheta}, \qquad Pr = \frac{a_T}{\vartheta},$$

$$Sc = \frac{a_C}{\vartheta}, \qquad Gr_T = \frac{g\beta_T L^3(T_0 - T_\infty)}{\vartheta^2}, \quad Gr_C = \frac{g\beta_C L^3(C_0 - C_\infty)}{\vartheta^2}, \qquad Ri = \frac{|Gr|}{Re^2}.$$

Thus, (3.7) – (3.10) become (3.11) – (3.14).

$$\frac{\partial U}{\partial X} + \frac{\partial V}{\partial Y} = 0 \tag{3.11}$$

$$U\frac{\partial U}{\partial X} + V\frac{\partial U}{\partial Y} = Ri(\theta - \chi)\sin\alpha + \frac{1}{Re}\left(\frac{\partial^2 U}{\partial Y^2}\right) \tag{3.12}$$

$$\frac{Uf}{K}\frac{\partial \theta}{\partial X} + \left(V - YL\frac{f'}{f}U\right)\frac{\partial \theta}{\partial Y} = \frac{1}{Pr}\frac{1}{Re}\frac{1}{L}\frac{\partial^2 \theta}{\partial Y^2} \tag{3.13}$$

$$\frac{Uf}{K}\frac{\partial \chi}{\partial X} + \left(V - YL\frac{f'}{f}U\right)\frac{\partial \chi}{\partial Y} = \frac{1}{Sc}\frac{1}{Re}\frac{1}{L}\frac{\partial^2 \chi}{\partial Y^2} \tag{3.14}$$

Boundary conditions are given below if at the wall $Y = 0$,

$$U = 0\,,$$

$$\theta = 1\,,$$

and

$$\chi = 1.$$

and if far from the wall $Y \to \infty$,

$$U \to 1\,,$$

$$\theta \to 0\,,$$

and

$$\chi \to 0\,.$$

3.3. Discretization of the Equations Using the Implicit Finite Difference Method

We have chosen the mesh shown in Figure 3 to apply the finite difference method to (3.11) – (3.14).

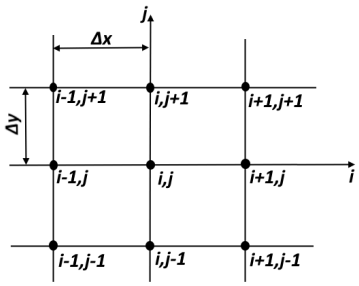

Figure 3. Mesh adopted for the numerical schemes

We obtain (3.15) – (3.18).

$$V_{i+1,j+1} = V_{i+1,j} - \frac{\Delta y}{\Delta x}\left(U_{i+1,j+1} - U_{i,j+1}\right) \tag{3.15}$$

$$Ri\left(\theta_{i,j} - \chi_{i,j}\right)\sin\alpha + U_{i,j}\frac{U_{i,j+1}}{\Delta x} = \left(-\frac{1}{Re\Delta y^2}\right)U_{i+1,j-1} + \left(\frac{2}{Re\Delta y^2} - \frac{V_{i,j}}{\Delta y}\right)U_{i+1,j} + \left(\frac{U_{i,j}}{\Delta x} + \frac{V_{i,j}}{\Delta y} - \frac{1}{Re\Delta y^2}\right)U_{i+1,j+1} \tag{3.16}$$

$$\frac{f}{K}\frac{U_{i,j}}{\Delta x}\theta_{i,j+1} = \left(-\frac{1}{PrReL\Delta y^2}\right)\theta_{i+1,j-1} + \left(\frac{2}{PrReL\Delta y^2} - \frac{V_{i,j}}{\Delta y} + YL\frac{f'}{f}U_{i,j}\right)\theta_{i+1,j} + \left(\left(\frac{f}{K} - YL\frac{f'}{f}\right)\frac{U_{i,j}}{\Delta x} + \frac{V_{i,j}}{\Delta y} - \frac{1}{PrReL\Delta y^2}\right)\theta_{i+1,j+1} \tag{3.17}$$

$$\frac{f}{K}\frac{U_{i,j}}{\Delta x}\chi_{i,j+1} = \left(-\frac{1}{ScReL\Delta y^2}\right)\chi_{i+1,j-1} + \left(\frac{2}{ScReL\Delta y^2} - \frac{V_{i,j}}{\Delta y} + YL\frac{f'}{f}U_{i,j}\right)\chi_{i+1,j} + \left(\left(\frac{f}{K} - YL\frac{f'}{f}\right)\frac{U_{i,j}}{\Delta x} + \frac{V_{i,j}}{\Delta y} - \frac{1}{ScReL\Delta y^2}\right)\chi_{i+1,j+1} \tag{3.18}$$

Boundary conditions are given at the wall $\eta = 0$ and $j = 1$,

$$U_{i+1,1} = 0\ ,$$

$$\theta_{i+1,1} = 1\ ,$$

and

$$\chi_{i+1,1} = 1$$

and far from the wall $\eta \to \infty$ and $j \to \infty$,

$$U_{i+1,\infty} \to 1\ ,$$

$$\theta_{i+1,\infty} \to 0\ ,$$

and

$$\chi_{i+1,\infty} \to 0\ .$$

To each numerical scheme of the discretized (3.15) – (3.18), we applied the consistency criterion of (3.19) and the stability criteria of relation (3.20), respectively, for the dimensionless velocity, temperature and concentration [23].

$$\lim_{\substack{\Delta x \to 0 \\ \Delta y \to 0}} \varepsilon_T = 0 \tag{3.19}$$

$$\left|\frac{\max\left(F_{i,j+1}-F_{i,j}\right)}{\max(F_{i,j+1})}\right| \leq 0.0001 \tag{3.20}$$

According to Lax's theorem [23], a consistent and stable numerical scheme is a convergent numerical scheme.

3. 4. Exchange Coefficients

For mixed convection, the exchange coefficients are the friction coefficient, the Nusselt number, and the Sherwood number. They characterize the quality of the flow velocity, the heat transfer velocity, and the mass transfer velocity, respectively, according to (3.21) – (3.23).

$$C_{f\,i+1,j+1} = \frac{2}{ReU_{i,j}}\frac{1}{f_{i+1}}\frac{1}{\Delta y}\left(\frac{U_{i+1,j+1}-U_{i+1,j}}{K}\right)_{\eta=0} \tag{3.21}$$

$$Nu_{i+1,j+1} = X\frac{-\frac{1}{f_{i+1}}\left(\frac{\theta_{i+1,j+1}-\theta_{i+1,j}}{\Delta y}\right)_{\eta=0}}{T_0-T_\infty} \tag{3.22}$$

$$Sh_{i+1,j+1} = X\frac{-\frac{1}{f_{i+1}}\left(\frac{\chi_{i+1,j+1}-\chi_{i+1,j}}{\Delta y}\right)_{\eta=0}}{C_0-C_\infty} \tag{3.23}$$

4. Results and Discussion

The results of the MATLAB numerical simulations of the discretized equations are presented in this section. We varied the following parameters: plate inclination, wavelength, and wave amplitude. We will visualize the variation of the U, θ, and χ distributions along the plate, as well as the heat transfer coefficients: the friction coefficient, the Nusselt number, and the Sherwood number.

We chose the value of Re = 300 in order to preserve the laminar description of the flow. We obtain the fluid velocity at the inlet of the plate using the expression for the Reynolds number and therefore the fluid velocity at the inlet and away from the plate $u_\infty = 9.42\ mm/s$. It is the same for the value of Ri =1 to remain in the phenomenon of mixed convection, without preponderance of natural convection or forced convection. The heat flux density is imposed $q = 100W/m^2$ as well as the temperature and concentration at the entrance and far from the plate $T_\infty = 293K$ and $C_\infty = 150mol/L$. The temperature and concentration at the wall are determined from formula 1.9 and the boundary conditions. For the steps, we chose Δx = 0.02 and Δy =0.02.

4.1. Results on Mixed Convection Parameters

For the figures in this section, one of the three parameters, α, L_0, and A_0, was varied to visualize its effects on the phenomenon. We began with α, for which the L_0 and A_0, were fixed. We began with the dimensionless velocity, then the dimensionless temperature, and finally the dimensionless concentration.

4.1.1. Dimensionless Velocity Results

Figures 4, 5, and 6 present the U distribution for different values of α, L_0, and A_0, respectively. The dimensionless variables X and Y are plotted on the x-axis and y-axis, respectively.

In Figures 4 (a), (b), and (c), we fixed L_0 at π/12 and A_0 at 0.025. α value changes from π/6, π/12 and π/24 respectively. Figure 4 (d) shows the percentages of the areas affected by the U distribution at different values of X and different values of α.

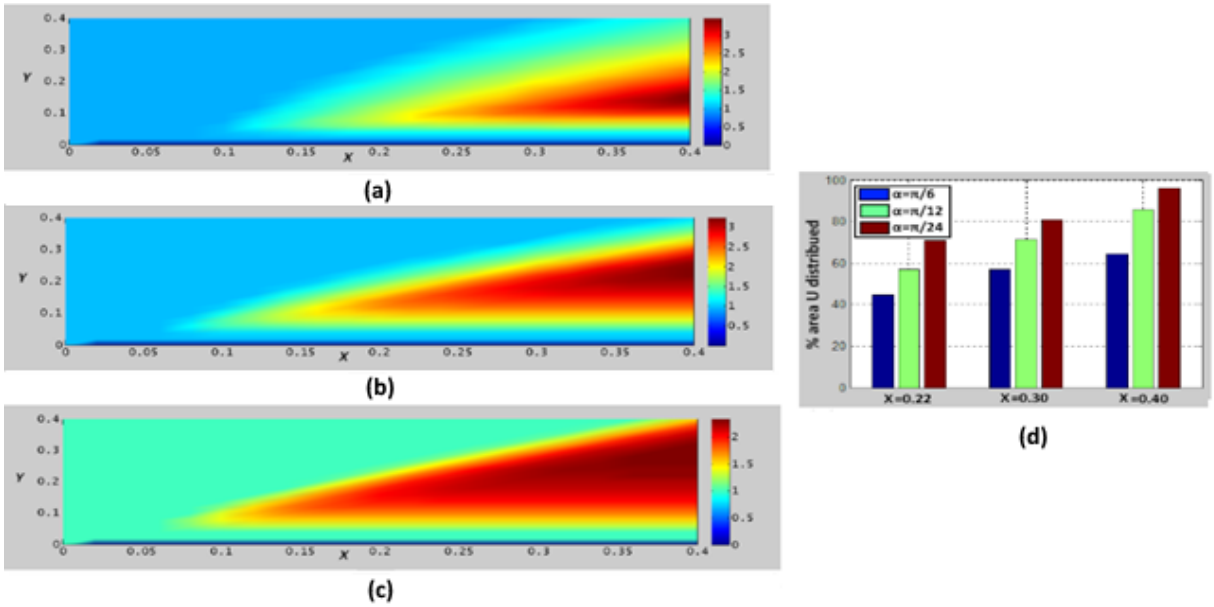

Figure 4. U distribution for $L_0 = \pi/12$, $A_0 = 0.025$ and different values of α:(a) α = π/6, (b) α = π/12, (c) α = π/24, (d) different values of X and α

In Figures 5 (a), (b), and (c), we set A_0 to 0.025 and α to π/6. For the L_0, we have π/3, π/6, π/12, respectively. Figure 5 (d) shows a comparison of the areas affected by the U distribution for different values of X and L_0.

In Figures 6 (a), (b), and (c), we fixed L_0 at π/12, and the α at π/6, and we varied A_0 by 0.015, 0.025, and 0.05. Figure 6 (d) shows the percentages of areas affected by the U distribution for different values of X and A_0.

4.1.2. Dimensionless Temperature Results

As for the U distribution, we have the dimensionless variables X and Y, the x-axis and y-axis, respectively, for the θ distribution. To visualize the effect of α on θ distribution, we set L_0 to π/12 and A_0 to 0.025. α corresponds to π/6, π/12, and π/24, respectively, in Figures 7 (a), (b), and (c). Figure 7 (d) shows the evolution of the percentages of areas affected by the θ distribution for different values of X and α.

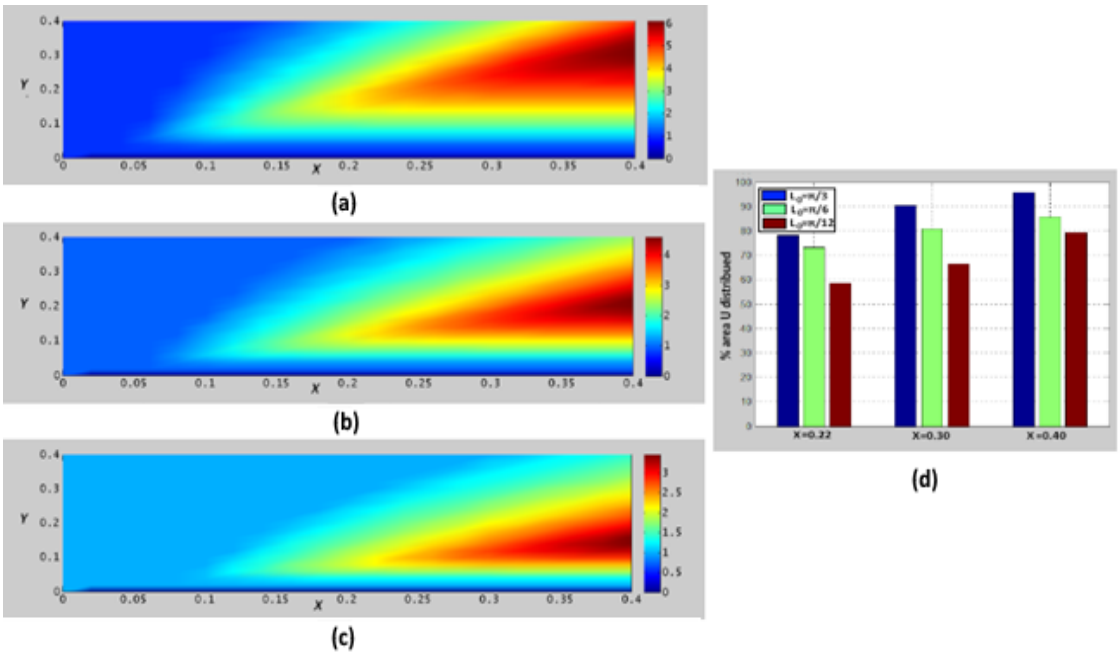

Figure 5. U distribution for $A_0 = 0.025$, $\alpha = \pi/6$ and different values of L_0: (a) $L_0 = \pi/3$, (b) $L_0 = \pi/6$, (c) $L_0 = \pi/12$, (d) different values of X and L_0

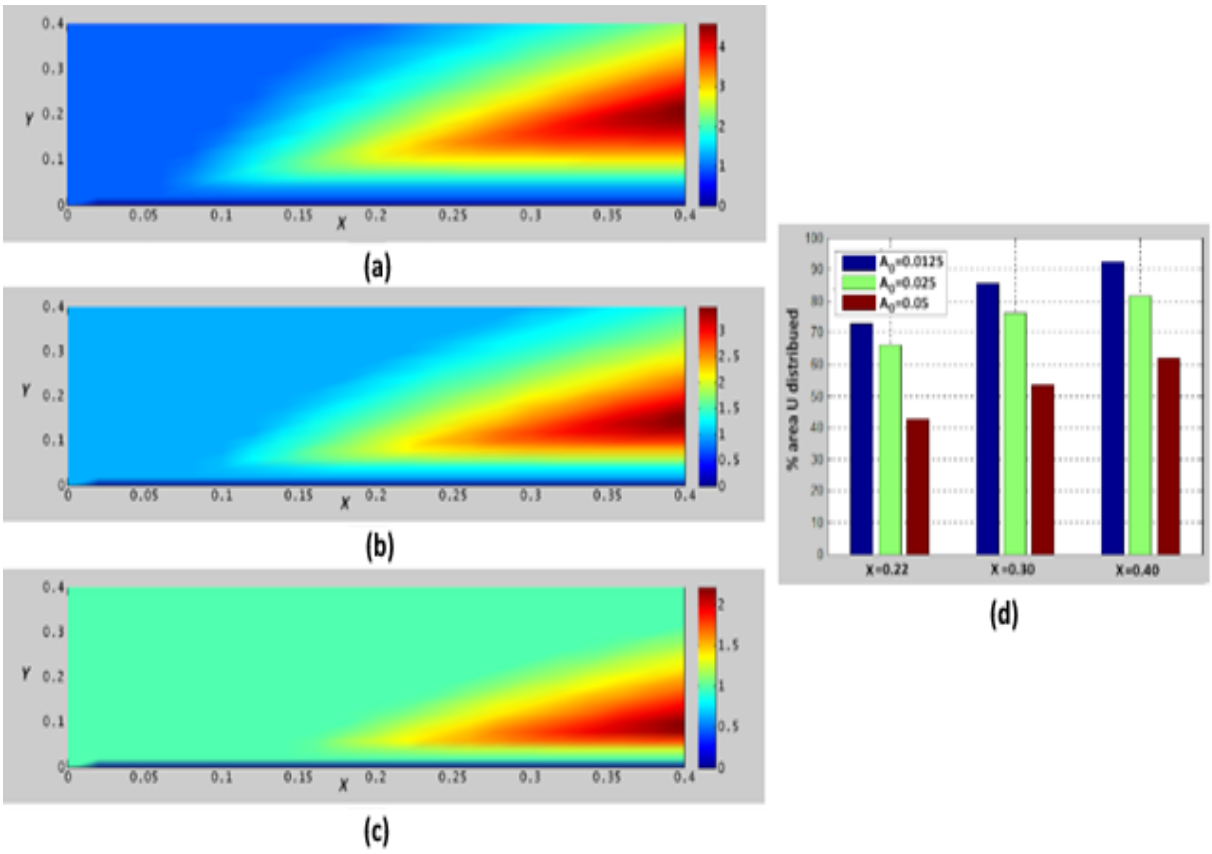

Figure 6. U distribution for $L_0 = \pi/12$, $\alpha = \pi/6$ and different values of A_0:(a) $A_0 = 0.0125$, (b) $A_0 = 0.025$, (c) $A_0 = 0.05$, and (d) different values of X and A_0

A_0 is set to 0.025 and the α to π/12 to visualize the effect of L_0 on θ distribution. This parameter changes from π/3, π/6, and π/12, respectively, in Figures 8 (a), (b), and (c). Figure 8 (d) shows the percentages of areas affected by the θ distribution for different values of X and L_0.

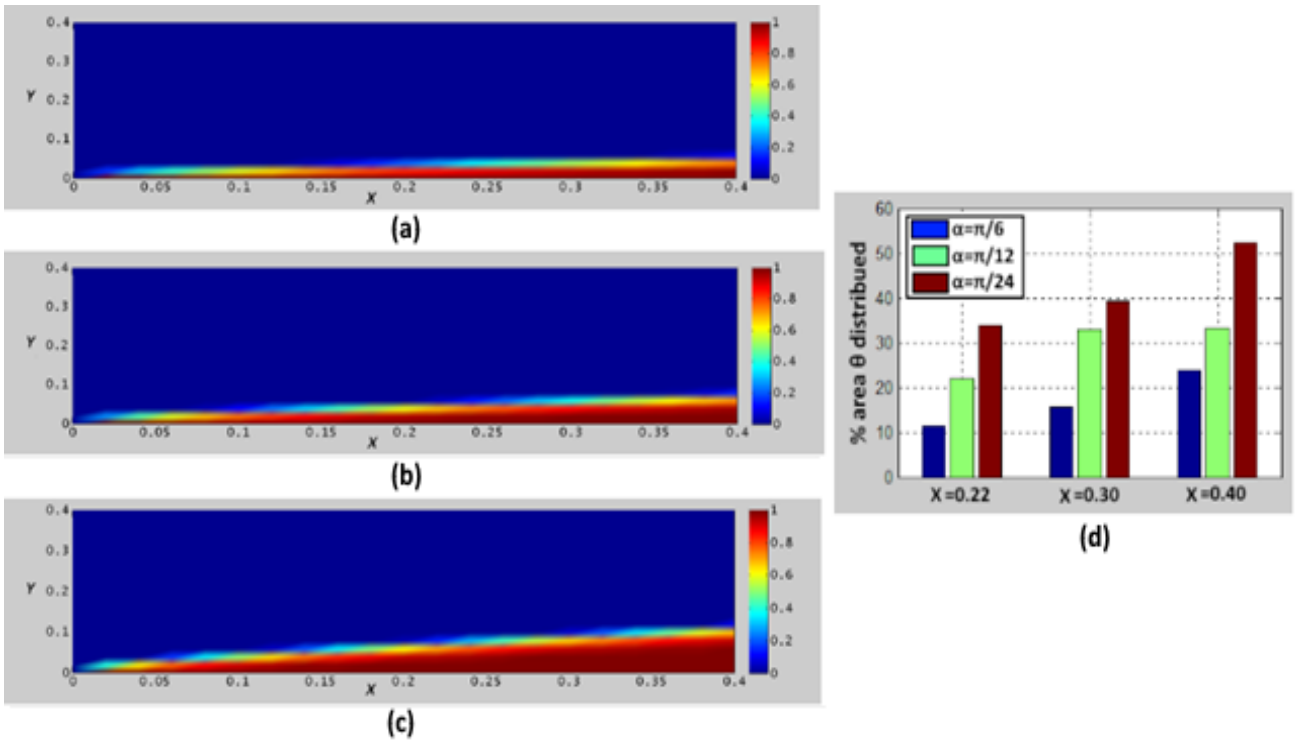

Figure 7. θ distribution for $L_0 = \pi/12$, $A_0 = 0.025$ and different values of α:(a) α = π/6, (b) α = π/12, (c) α = π/24, (d) different values of X and α

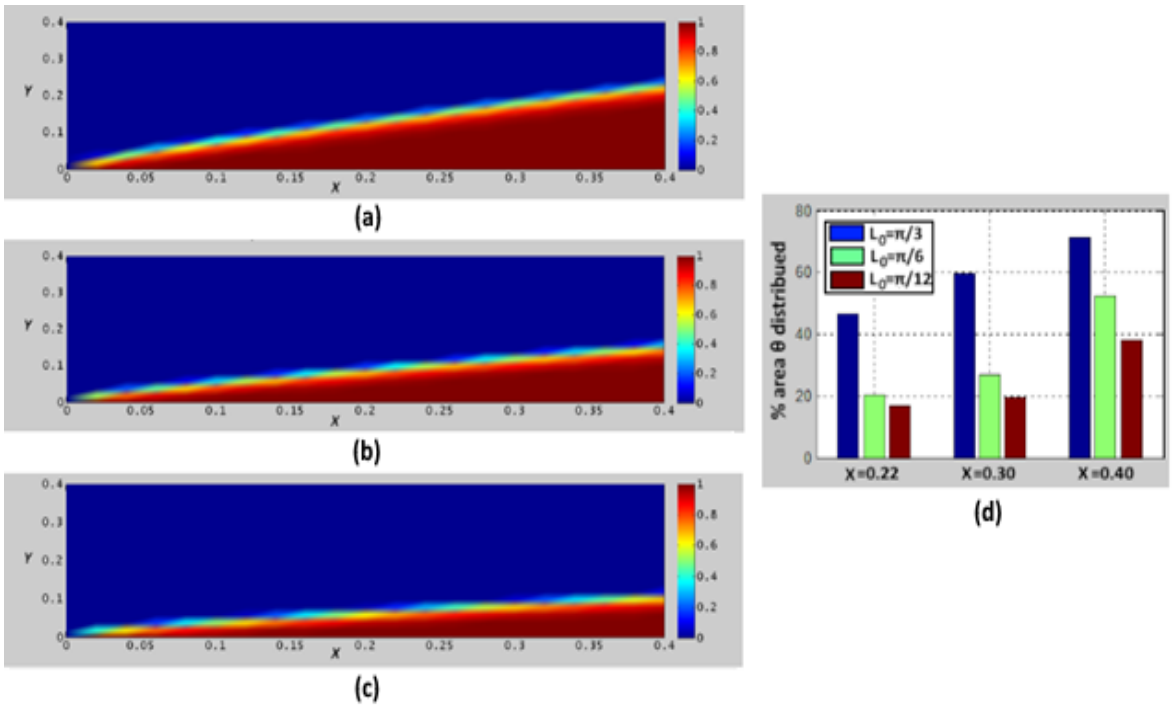

Figure 8. θ distribution for $A_0 = 0.025$, $\alpha = \pi/12$ and different values of L_0:(a) $L_0 = \pi/3$, (b) $L_0 = \pi/6$, (c) $L_0 = \pi/12$, (d) different values of X and L_0

We varied A_0 to 0.0125, 0.025, 0.05, and 0.1 in Figures 9 (a), (b), and (c). On the other hand, L_0 is fixed at π/6 and the α at π/12. Figure 9 (d) summarizes the percentage of areas affected by the θ distribution for different values of X and A_0.

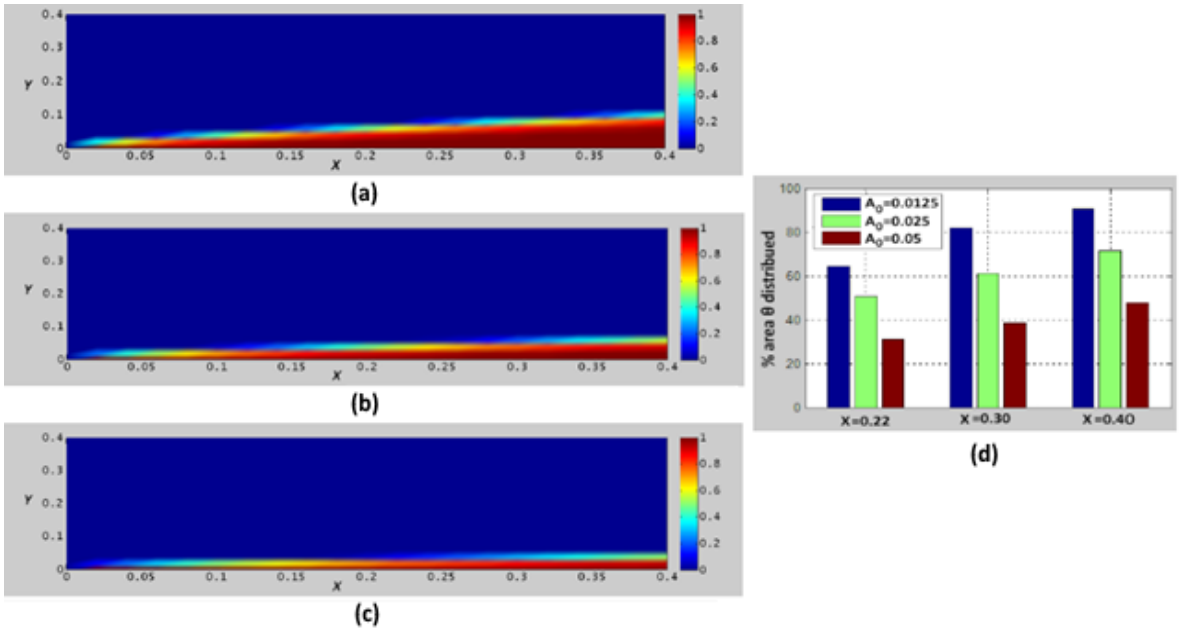

Figure 9. θ distribution for $L_0 = \pi/6$, $\alpha = \pi/12$ and different values of A_0:(a) $A_0 = 0.0125$, (b) $A_0 = 0.025$, (c) $A_0 = 0.05$, and (d) different values of X and A_0

4.1.3. Dimensionless Concentration Results

Here we present the results on the dimensionless concentration by varying the following parameters individually: α, L_0, and A_0. On the x-axis, we have the dimensionless variables X and Y for the y-axis in Figures 10, 11, and 12.

In Figures 10 (a), (b), and (c), we have the χ distribution for αvalues: π/3, π/6, π/12, and π/24, respectively. L_0 is fixed at π/12 and A_0 at 0.025. Figure 10 (d) illustrates the percentage of χ distribution for different values of X and α.

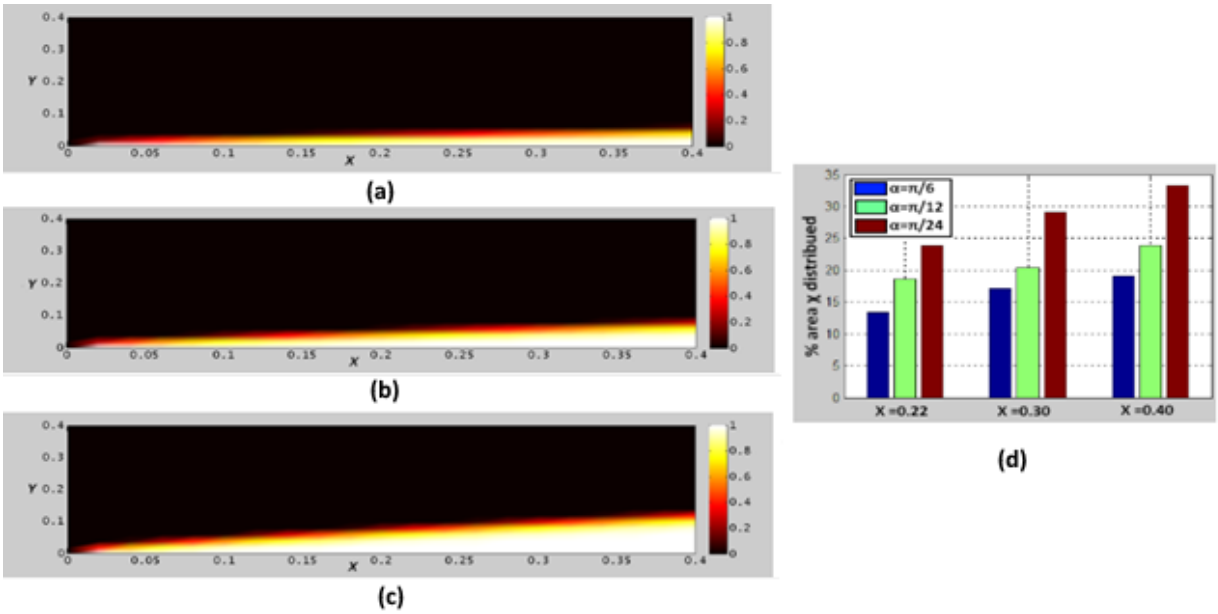

Figure 10. χ distribution for $L_0 = \pi/12$, $A_0 = 0.025$ and different values of α:(a) α = π/6, (b) α = π/12, (c) α = π/24, (d) different values of X and α

To highlight the effects of L_0 on χ distribution, we fixed the values of A_0 at 0.025 and α at π/12. We varied L_0 by π/12, π/8, and π/6 in Figures 11 (a), (b), and (c). Figure 11 (d) highlights the variation of the areas affected by the χ distribution for different values of X and L_0.

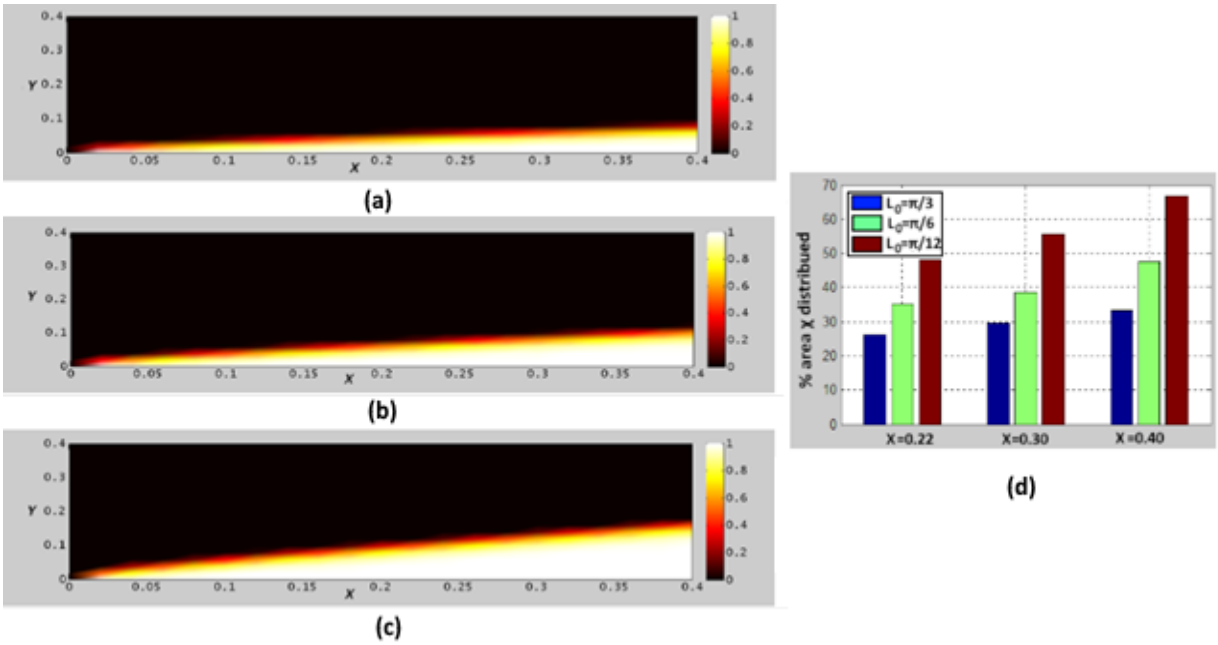

Figure 11. χ distribution for $A_0 = 0.025$, $\alpha = \pi/12$ and different values of L_0: (a) $L_0 = \pi/3$, (b) $L_0 = \pi/6$, (c) $L_0 = \pi/12$, (d) different values of X, and L_0

The effect of A_0 is highlighted in Figures 12 (a), (b), and (c), where its values change from 0.025, 0.05, 0.1, and 0.2 respectively. L_0 is fixed at π/6 and α at π/24. Figure 12 (d) shows the evolution of the areas concerned by the χ distribution for different values of X and A_0.

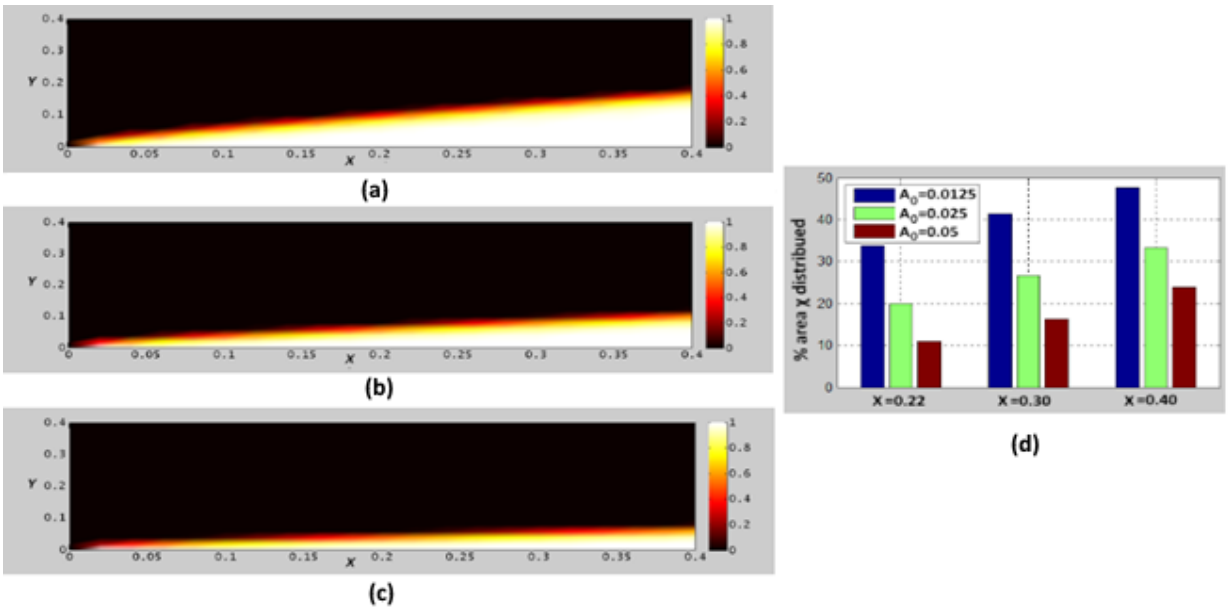

Figure 12. χ distribution for $L_0 = \pi/6$, $\alpha = \pi/24$, and different values of A_0:(a) $A_0 = 0.0125$, (b) $A_0 = 0.025$, (c) $A_0 = 0.05$, and (d) different values of X, and A_0

4.2. Exchange Coefficients Results

The heat exchange coefficients are the friction coefficient, the Nusselt number, and the Sherwood number. They characterize the quality of the flow velocity, the heat transfer velocity, and the mass transfer velocity, respectively. As with the mixed convection parameters, we varied the wavelength, wave amplitude, and plate inclination individually to determine their influence on the heat exchange coefficients.

4.2.1. Friction Coefficient Results

Cfx results are presented in Figures 13 (a), (b), and (c). They correspond to Cfx variations for different values of α, L0, and A0, respectively. We have the dimensionless variable Y on the x-axis and Cfx on the y-axis.

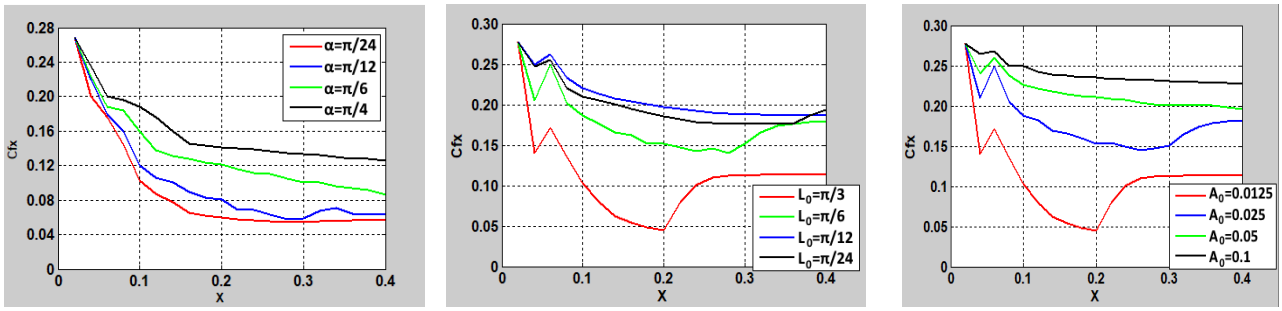

(a) (b) (c)

Figure 13. Cfx variation for different values of (a) α, (b) L_0, and (c) A_0

4.2.2. Nusselt Number Results

Figures 14 (a), (b), and (c) show the Nu variations as a function of α, L_0, and A_0, respectively. Nu represents the y-axis, and the dimensionless variable X represents the x-axis. In Figure 14 (a), we have Nu variations as a function of α, which changes from $\alpha = \pi/24$, $\pi/12$, $\pi/6$, and $\pi/4$, respectively. In Figure 14 (b), Nu varies according to $L_0 = \pi/3$, $L0 = \pi/4$, $L_0 = \pi/6$, and $L_0 = \pi/12$. In Figure 14 (c), we varied $A_0 = 0.0125$, $A_0 = 0.025$, $A_0 = 0.05$, and $A_0 = 0.1$ to visualize the effects on Nu.

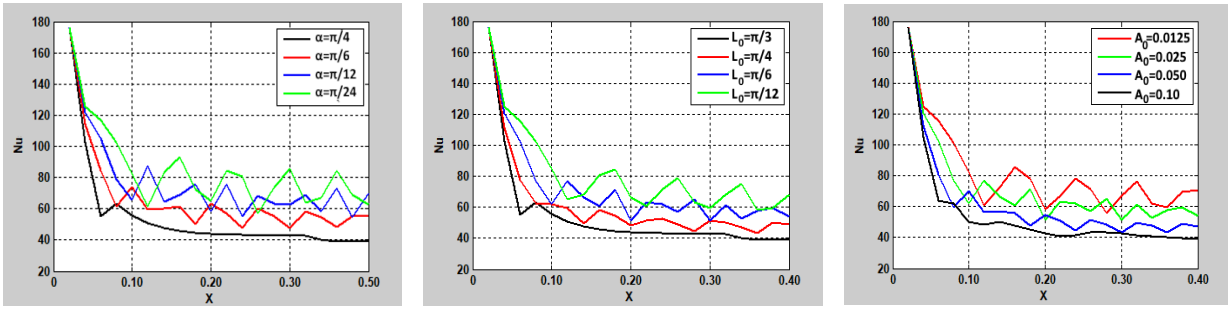

(a) (b) (c)

Figure 14. Nu variation for different values of (a) α, (b) L_0, and (c) A_0

4.2.3. Sherwood Number Results

Sh variations are presented in Figures 15 (a), (b), and (c). Sh changes along the y-axis and varies with the dimensionless variable Y on the x-axis. Figures 15 show the effects of α, L_0, and A_0 on Sh, respectively. The value of α varies from π/24, π/12, π/6, and π/4. We varied the L_0 from π/3, π/4, π/6, and π/12. For A_0, its value changes from 0.0125, 0.025, 0.50, and 0.1.

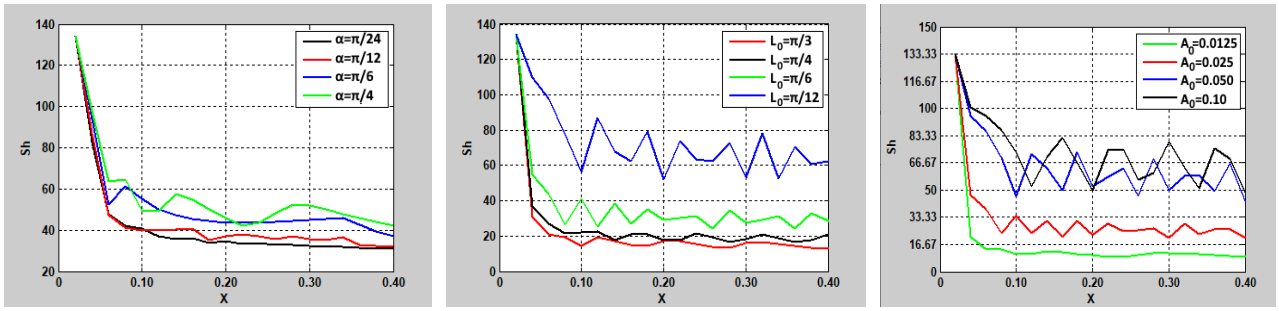

(a) (b) (c)

Figure 15. Sh variation for different values of (a) α, (b) L_0, and (c) A_0

4.2.4. Unstable results on the dimensionless velocity distribution

Figures 16 to 19 present examples of unstable U distribution. We only change one parameter among Re, Ri, Δx, and Δy according to Table 5. For example, for Figure 16, we chose Δx = 0.4 instead of 0.02, and the stability of the discretized equations was called into question. In Figure 17, we chose Δy = 0.2 instead of 0.02. In Figure 18, we chose Re=3000 instead of 300. In Figure 19, we chose Ri = 0.1 instead of 1. For α, L_0 and A_0, we stayed respectively in the intervals [π/24 ; π/3], [π/24 ; π/3], and [0.0125 ; 0.1].

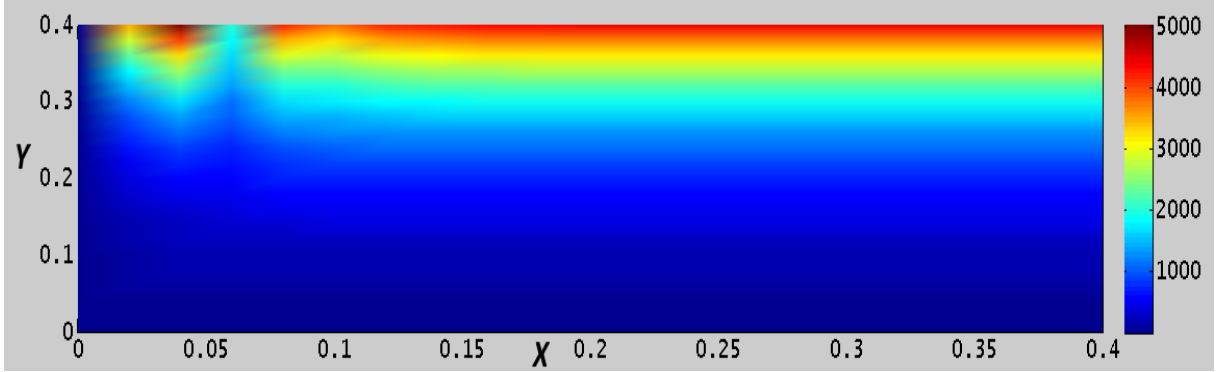

Figure 16. Unstable U distribution for Δx = 0.4, Re = 300, Ri = 1 and Δy = 0.02

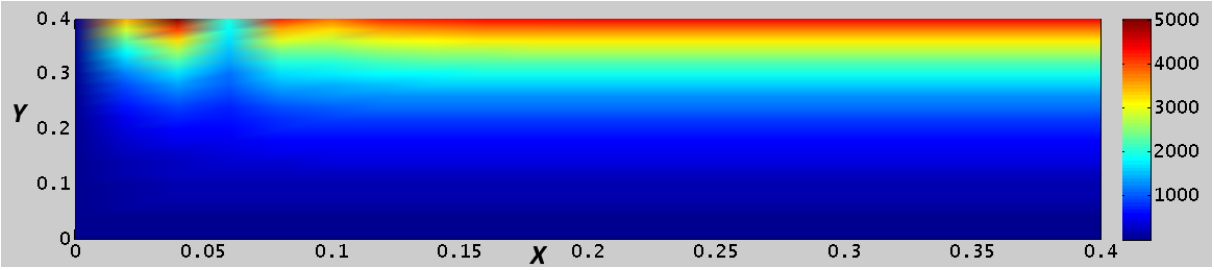

Figure 17. Unstable U distribution for Δy = 0.2, Δx = 0.02, Re = 300, and Ri = 1

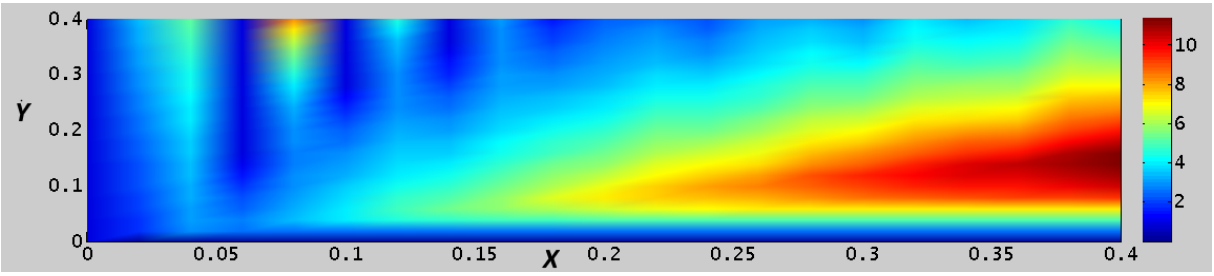

Figure 18. Unstable U distribution for Re =30000, Δx = 0.02, Δy = 0.02, and Ri = 1

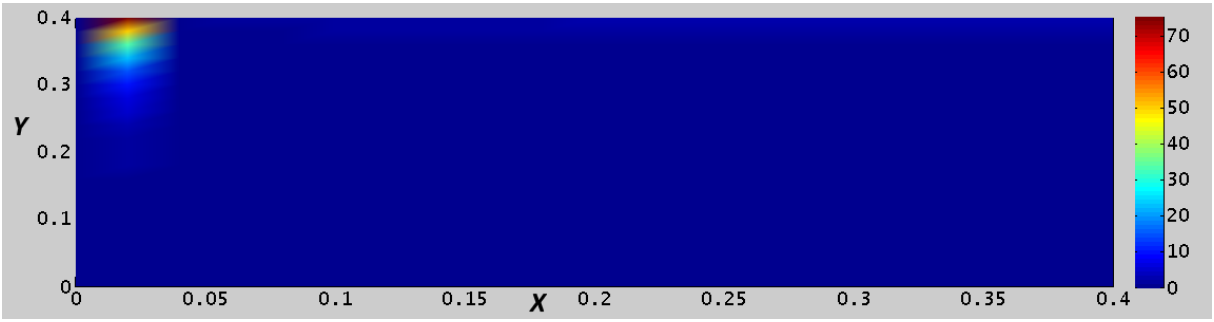

Figure 19. Unstable U distribution for Ri = 0.1, Re = 300, Δx = 0.02 at Δy = 0.02

4.3. Discussion

4.3.1. Discussion on Mixed Convection Parameters

We have chosen the wavelength values π/24, π/12, π/6, π/4, and π/3, which are particular angles expressed in radians. In order to simplify the radian dimension in the sine function that describes the plate undulation, we have opted for these wavelength values. For the wave amplitude values, they are expressed in meters and are chosen so as not to have deep undulations that are characterized as sources of fluid recirculation zone. We chose the intervals [0;0.4] for the dimensionless variables because they are sufficient to illustrate the variations of the dimensionless quantities: U, θ, and χ for different values of α, L_0, and A_0. We narrowed the Y axis relative to the X axis for better visibility of the three types of boundary layers: dynamic, thermal, and mass.

Figure 4 indicates that decreasing α leads to an increase in U distribution. We see that there are more areas affected by U distribution as α increases. For example, for X = 0.22, we see the area affected by U distribution increase by 43%, 58%, and 70%, respectively, for α = π/6, α = π/12, and α = π/24. These percentages are measured relative to the value of 0.4 for Y. When X=0.4, the percentage of areas affected by U distribution reaches 96% for α = π/24. In Figure 4 (a) for α = π/6, the value of U reaches 3.4 at the core of the boundary layer, compared to 3.1 for α = π /12 and 2.3 for α = π /24. Figures 4 (a), (b), and (c) also show that decreasing α accelerates the flow. Figures 4 reflect the results of our previous study [24] that decreasing α causes the increase in U distribution, on an inclined flat plate. The same effects are also recorded on the variations of θ and χ for different values of α.

In Figures 5, we notice that the decrease in L_0 causes the decrease in U distribution. Figure 5 (d) clearly shows that there are fewer areas affected by U distribution when L_0 decreases. For example, for X = 0.30, the percentages of these areas increase from 90%, 81%, 76% for $L_0 = \pi/3$, $\pi/6$, and $\pi/12$, respectively. Figures 5 (a), (b), and (c) show that the decrease in L_0 slows down the flow. In Figure 5 (a) for L_0 = π /3, the value of U reaches 6 at the heart of the boundary layer, drops to 4.3 for $L_0 = \pi/6$ and to 3.5 for $L_0 = \pi/12$. In Figure 6, the effect of increasing A_0 is the decrease in the U distribution. The percentage of areas affected by this distribution varies from 92%, 81%, 63% when A_0 going from 0.0125, 0.025, and 0.05. In Figures 6 (a), (b), and (c), increasing A_0 tends to slow down the flow. We have a maximum value of U of 4.4 for $A_0 = 0.0125$. It drops to 3.4 for $A_0 = 0.025$ and to 2.2 for $A_0 = 0.05$. Figures 4-6 allow us to conclude that increasing α and A_0 tend to disadvantage U distribution. On the other hand, increasing L_0causes the opposite effect.

In Figures 4 (d) and 6 (d), the increase in the percentages of areas affected by U distribution can be associated with the thickening of the dynamic boundary layer. This results in the promotion of fluid movement on the wall. In Figure 5 (d), we see the opposite phenomenon: the thinning of the dynamic boundary layer by the decrease in L_0. The results of G. Brillant et al. [25] allow us to validate our results on the U distribution, which are summarized in Table 2.

Table 2. Cross-study effects on dimensionless velocity distribution comparison

Study	Variables	Effects	Software used
Present study	α, L_0, A_0	Increasing α and A_0 adversely affects the speed distribution, increasing L_0 causes the opposite effect	MATLAB
[25]	F : injected fluid rate	Increasing F leads to increasing the velocity distribution	ANSYS FLUENT

Figures 7 (a), (b), and (c) show that there are more areas affected by θ distribution when α decreases. This results in better heat exchange between the fluid and the wall. Figure 7 (d) quantifies this phenomenon more precisely. For example, we observe a percentage of θ distribution areas that increases from 24%, 33% to 52% respectively for $\alpha = \pi/6$, $\alpha = \pi/12$, and $\alpha = \pi/24$. Analysis of Figures 8 (a), (b), and (c) allows us to say that the decrease in leads to a decrease in θ distribution. In Figure 8 (d), $L_0 = \pi/3$, the percentage of areas affected by the distribution increases from 45%, 59% to 69% respectively for X = 0.22, X = 0.30, and X = 0.40.

The effects of varying A_0 on θ distribution are shown in Figures 9 (a), (b), and (c). As we increase A_0, the areas affected by θ distribution become thinner. Figure 9 (d) shows that for A_0 increasing from 0.0125, 0.025 to 0.05, the percentage affected by θ distribution decreases from 82%, 61% to 39% for X = 0.30. We can say that increasing A_0 reduces the thickness of the thermal boundary layer, and therefore the quality of heat exchange between the fluid and the wall.

The work of G. Brillant et al [25], illustrated in Figures 20 and 21, validates our results on the θ distribution. These researchers visualized the effect of the fluid injection rate on θ distribution on Ansys Fluent. The increase in this injection rate is accompanied by the thickening of the thermal boundary layer.

Figures 10 (a), (b), and (c) show that we have a better χ distribution when we decrease α. We see a wider mass boundary layer and therefore a favored mass transfer. Figure 12 (d) reinforces this observation as for X = 0.22, we see the percentage of areas affected by χ distribution increase from 13%, 18% to 24% when we vary α respectively from π/6, π/12 to π/24. Figures 11 (a), (b), and (c) indicate that decreasing the disadvantages of the χ distribution. For X = 0.40, the areas affected by χ distribution are 33%, 48% and 67% respectively for L_0 equal to π/3, π/6 to π/12. Therefore, the mass boundary layer thickens with the decrease of L_0. Figures 12 (a), (b), and (c) show that decreasing A_0 also leads to a thickening of the mass boundary layer. For X = 0.22,

only 11% of Y is affected by the χ distribution for $A_0 = 0.05$, compared to 20% for $A_0 = 0.025$ and 33% for $A_0 = 0.0125$. Increasing A_0 thus tends to reduce the thickness of the mass boundary layer. Consequently, mass transfer is hindered by increasing A_0.

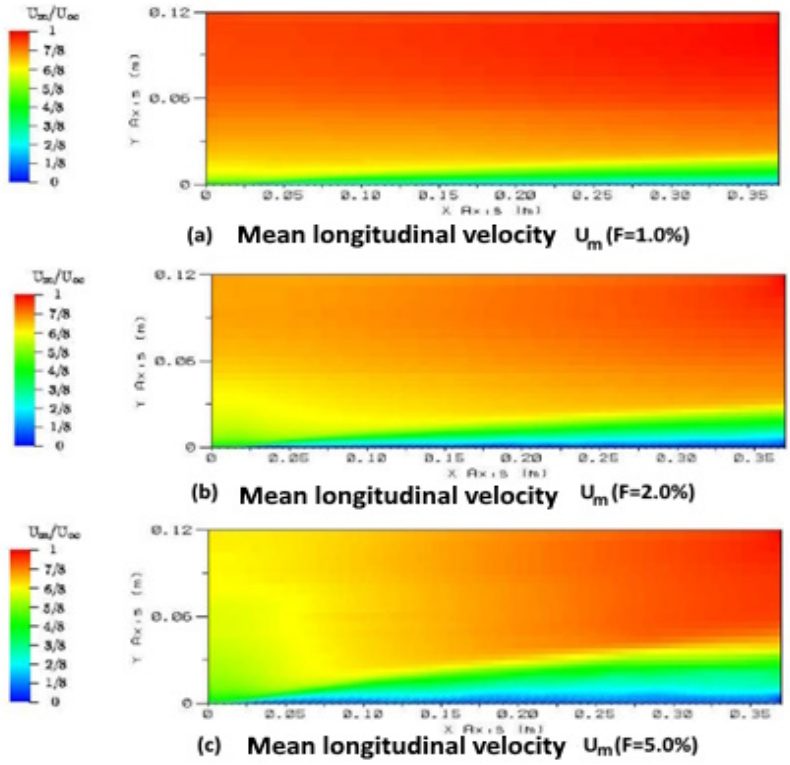

Figure 20. Distributions of the mean longitudinal velocity U_m for different values of F [25]

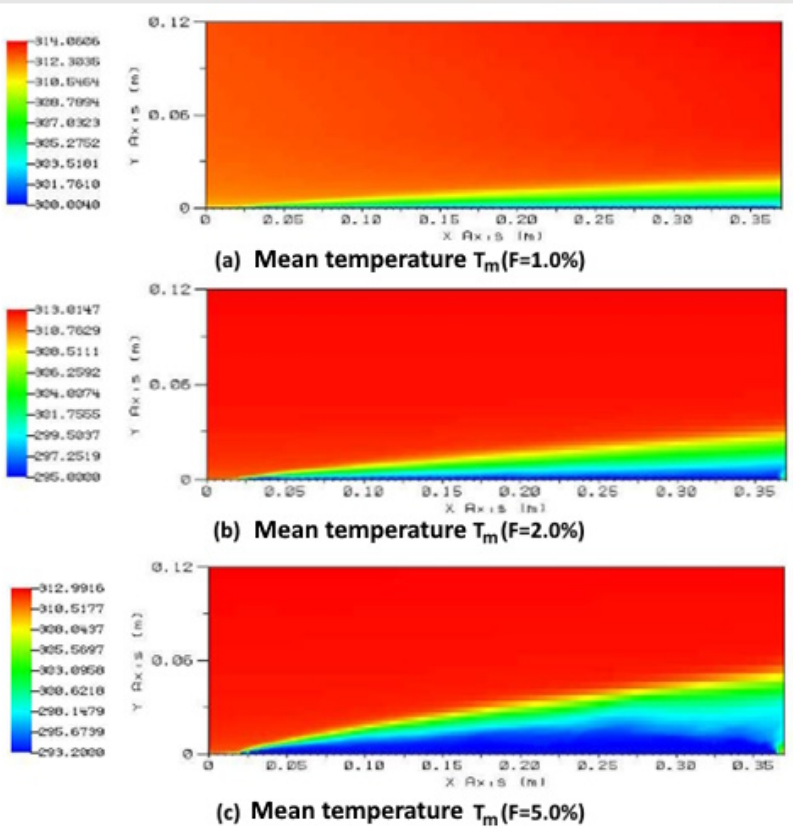

Figure 21. Dimensionless temperature variation for different values of the fluid injection rate F [25]

4.3.2. Discussion on Exchange Coefficients

Figure 13 (a) shows that increasing α leads to increasing Cfx. There is therefore more friction between the fluid and the wall, which tends to slow down the flow in the dynamic boundary layer as α increases. The ripples are closer together as we decrease L_0. This causes the Cfx values to increase, as the obstacles to flow are larger. The curve shapes in Figure 13 (b) indicate this phenomenon. As we increase A_0, the Cfx value also increases. There are more obstacles for the fluid to overcome, which results in flow resistance when the ripples are deeper. The curve profiles for $A_0 = 0.0125$, 0.025, 0.05, and 0.1 in Figure 13 (c) reinforce this effect.

We also see that the wavy shape of the wall influences the profiles of Cfx, those of Nu, and Sh. The friction between the fluid and the wall reaches lower values when L_0 is higher and A_0 is lower. The results of H. Guittoun [26] also confirm this phenomenon. In Figure 22, they compared the Cfx between a flat wall and a wavy wall at the 54th undulation, showing the tendency of the Cfx values to follow the wavy shape. Table 3 illustrates a comparison with this cross-analysis.

Table 3. Cross-study methodology comparison

Study	Geometry	Methodology	Tool
Present study	Inclined corrugated wall	Homotopic Transformation Adimensionalization Implicit Finite Difference Method	MATLAB
[26]	Lower corrugated wall channel	Finite Volume Method Computational Fluid Dynamics	Meshing with GAMBIT Simulation with ANSYS Fluent

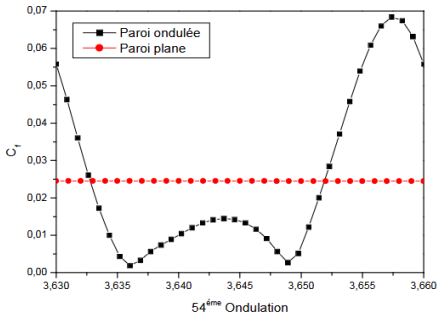

Figure 22. Variation of the friction coefficient by H. Guittoun and al [26]

Figures 14 and 15 are also validated by the results of H. Guittoun and al [26] in Figure 23 and those of M.S. Abdallah [27] in Figure 24. In Figures 14 (a) and 14 (c), respectively, the values of Nu decrease with the decrease of α and A_0. On the other hand, the increase of L_0 presents the same effect on Nu as in Figure 14 (b). In Figure 14 (a) $\alpha = \pi/4$ displays higher values of Nu than for $\alpha = \pi/6$, and this one is higher than those for $\alpha = \pi/12$. We thus have a better quality of heat exchange between the fluid and the wall when we increase α or A_0. In Figure 14 (b), we have higher Nu values for $L_0 = \pi/12$ than for $L_0 = \pi/6$, which also has higher Nu values than for $L_0 = \pi/3$. The increase in L_0 is thus associated with the reduction in the quality of heat exchange between the fluid and the wall. It is the same for Figure 14 (c) where the increase in A_0 leads to the reduction of Nu values. For example, A_0=0.0125 offers better heat exchange than $A_0 = 0.025$. The latter offers higher Nu values than $A_0 = 0.05$.

In Figure 15 (a), the values of Sh increase with those of α. It is the same in Figure 16 (c) where the values of Sh increase with those of A_0. This results in the improvement of the quality of mass exchange within the flow when α goes from π/24, π/12, π/6 to π/4 or when A_0 goes from 0.0125, 0.025, 0.050 to 0.1. The opposite effect

is caused by the increase of L_0 as shown in Figure 16 (b). By going from $L_0 = \pi/3, \pi/4, \pi/6$ to $\pi/12$, there will be a decrease in the quality of mass exchange within the flow.

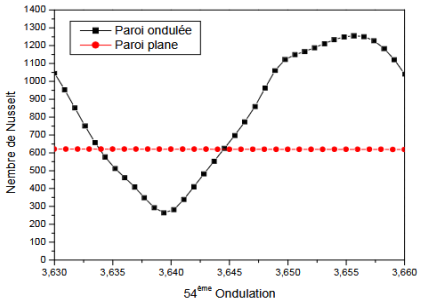

Figure 23. Variation of the Nusselt number for H. Guittoun and al [26]

By analogy in (2.22) and (2.23), the patterns of Nu and Sh variations are similar. Like Figures 14 and 15 are thus validated by Figures 23 [25]. M.S. Abdallah's results also highlight the effects of ripple on the Cfx and Nu exchange parameters in Figures 20–21 [27]. Table 4 summarizes the comparison with this study and ours.

Table 4. Cross-study effect of increasing wave amplitude comparison

Study	Geometry	Variable	Effect of increasing the variable
Present study	Inclined corrugated plate	A_0	Decrease of Cfx, Nu and Sh
[27]	Frustum of a cone with a sinusoidal wall	Wave amplitude	Decrease of Cfx and Nu

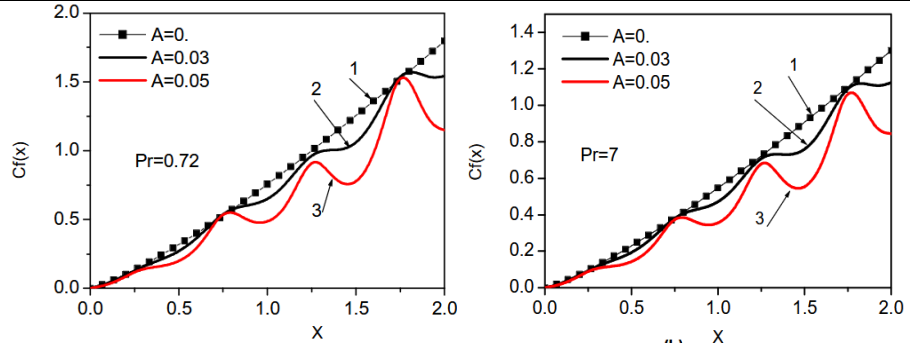

Figure 24. Evolution of the friction coefficient along the sinusoidal conical surface [27]

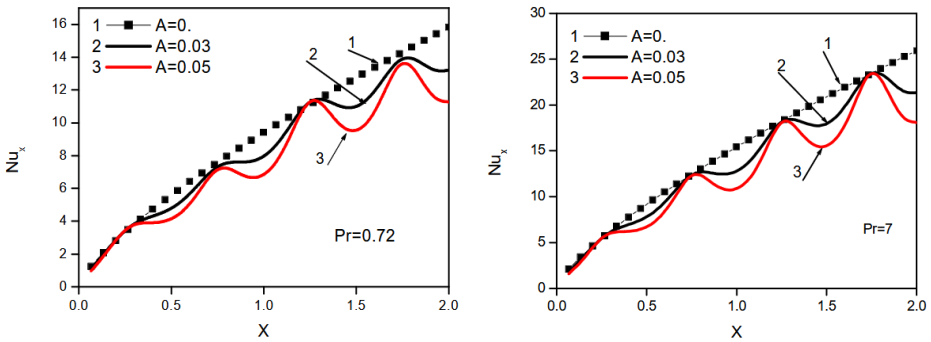

Figure 25. Evolution of the Nusselt number as a function of the amplitude along the sinusoidal conical surface [27]

The procedure: homotopic transformation, adimensionalization, implicit finite difference method to deal with the geometry problem in the presence of undulation has already been used before. The difference lies in the geometric form. Table 5 shows a comparison between the present study and that of [27].

Table 5. Cross-study homotopic transformation and the convergence criterion of the discretized equations comparison

Study	Geometric configuration	Homotopic transformation	Convergence criterion for discretized equations
Present study	Inclined corrugated plate	$x = \xi$ $y = \eta\, f(\xi)$	$\left\lvert \frac{max\left(F_{i,j+1} - F_{i,j}\right)}{max\ (F_{i,j+1})} \right\rvert \leq 0.0001$
[27]	Sinusoidal cone truncated	$\xi = X$ $\eta = \frac{Y - f(X)}{g(X) - f(X)}$	$\frac{\sum\lvert\phi_p^{k+1} - \phi_p^k\rvert}{\sum\lvert\phi_p^{k+1}\rvert} \leq 10^{-5}$

In all cases, the dynamic, thermal, and mass boundary layers thicken with increasing X. This verifies the theory that the thickness of the boundary layer thickens as one moves away from the leading edge [28]. This validates our programs on MATLAB for solving discretized equations. The boundary layer is the region near the wall in which a parameter varies significantly. The temperature varies significantly, for example, in the thermal boundary layer. The thicker it is, the greater the heat exchange between the fluid and the wall. This allows us to conclude on the improvement of exchanges within the fluid by analyzing the effects of increasing or decreasing the parameters α, L_0 and A_0.

4.3.3. Discussion on unstable results of dimensionless velocity distribution

Changing the value of one or more parameters in the computer program can lead to non-compliance with conditions 2.19 and 2.20. The choice of steps Δx and Δy, in the implicit finite difference method, has a significant impact on the consistency and stability of the equations, and therefore their convergence. Categorizing the values for which the results are unstable requires testing all possible values. This requires more time because the values are random up to this point. We propose that the flow tends toward a turbulent regime due to this unpredictable nature of the instability of the equations for certain values.

In Figure 18, we chose Re = 30000 to visualize the U distribution with $L_0 = \pi/12$, $A_0 = 0.025$, and α π/12. When Y→∞, U no longer tends towards 1. We also note that the value of U can reach 10 in certain regions. We observe U variations outside the dynamic boundary layer. These variations are even randomly localized. Figure 17 is another case of an unstable numerical scheme result for the U distribution when we changed the step size Δy = 0.2, even though we have the values of Re, Ri, and Δx according to Table 6. We note the disappearance of the boundary layer at the wall in Figures 16, 17, and 19. U values reach 5000 in some regions.

Table 6. Examples of parameter values for stable and unstable numerical schemes for U distribution

Parameters	Δx	Δy	Re	Ri
Stable	0.02	0.02	300	1
Unstable	**0.4**	0.02	300	1
Unstable	0.02	**0.2**	300	1
Unstable	0.02	0.02	**30000**	1
Unstable	0.02	0.02	300	**0.1**

Figure 19 presents an unstable result for U distribution when we chose Ri = 0.01, but the values of Re, Δx, and Δy are preserved. The objective of this choice is to visualize the result of the U distribution if forced convection were dominant over natural convection.

Δx, Δy, Re and Ri are dimensionless parameters, and are found in the discretized system of (2.15-2.18). Knowing from which values of Re or Δx for example, is not the objective of our study. Moreover, it would require more time and calculations. In any case, we can deduce that the increase of Re leads to the instability of the discretized schemes, hence the appearance of turbulence. It is the same concerning the increase in Δx or Δy, as well as the decrease in Ri. On the other hand, the decrease of Re, Δx or Δy tends to stabilize the numerical schemes. Indeed, the points for the calculations in the mesh are closer respecting the formula 2.20. As for the increase of Ri, this corresponds to the preponderance of natural convection, and this reinforces the stability of the luminary flow.

5. Conclusion

A two-dimensional study of mixed convection evaporation from an inclined corrugated plate was undertaken. We selected hypotheses and methods, and presented results that we were able to compare with other studies. Our results demonstrated the effects of plate inclination, wavelength, and wave amplitude on the parameters and heat exchange coefficients of mixed convection. Depending on the quantity studied, the three variables can generate the same effect, or two variables can have an inverse effect on the third variable. Increasing the wavelength leads to an increase in the U distribution within the flow. In contrast, increasing the wave amplitude and plate inclination causes the opposite effect. Reducing the plate inclination, lowering the wave amplitude, and increasing the wavelength promote heat transfer between the fluid and the wall, and within the fluid itself. These same effects are recorded for mass transfer between the wet wall and the fluid for the same variations of the three parameters. The variation of the friction coefficient as a function of the plate's undulation and inclination supports the phenomena recorded for the dimensionless velocity distribution. Furthermore, the Nusselt and Sherwood numbers concern the quality of the dimensionless temperature and concentration distributions. The choice of assumptions such as laminar flow regime or constant heat flux density is only a simplifying assumption for an inclined corrugated wall. For good reason, such geometry presents more complex realities, namely the appearance of turbulence even for low Reynolds number values. Finally, we presented results for which our system of discretized equations exhibits a dimensionless velocity distribution that is unstable. This is caused either by increasing the Reynolds number, x-step or y-step, or by decreasing the Richardson number.

Author Contributions

All the authors equally contributed to this work. They all read and approved the final version of the paper.

Conflict of Interest

All the authors declare no conflict of interest.

Ethical Review and Approval

No approval from the Board of Ethics is required.

References

[1] N. M. Rouai, Passive cooling in modern nuclear reactors (1998), https://inis.iaea.org/records/2hjaw-r3k53, Accessed 07 Jul 2025.

[2] K. Sidi-Ali, *Complex Fluid flow in power nuclear reactors cores; cases of BWR, PBMR and HTR-PM*, Acta Materialia Turcica 4 (3) (2020) 25–34.

[3] S. R. S. Dias, F. P. L. Futata, J. A. Carvalho Jr., H. S. Couto, M. A. Ferreira, *Investigation of food grain drying with pulsating air flows,* International Communications in Heat and Mass Transfer 31 (3) (2004) 387–395.

[4] S. Akçay, U. Varghese, *Mixed convention heat transfer from a vertical flat plate subjected to periodic oscillations,* Journal of Thermal Engineering 7(6) (2021) 1377-1391.

[5] M. M. A. Klazly, G. Bognar, *Computational fluid dynamic simulation of laminar flow over a flat plate*, Design of Machines and Structures 9 (1) (2019) 29–47.

[6] M. A. Kassim, Etude numérique et expérimentale des transferts couplés de chaleur et de masse en convection mixte dans un canal (2010), https://toubkal.imist.ma/xmlui77/handle/123456789/9780, Accessed 07 Jul 2025.

[7] O. Kholai, A. Bellaouar, M. Kadja, Etude numérique de la convection mixte dans un tube incline (2007), https://hal.archives-ouvertes.fr/hal-00160479, Accessed 07 Jul 2025.

[8] Z. Anxionnaz, *Etude de l'influence de la géométrie des canaux sur les performances d'un réacteur/échangeur*, Doctoral Dissertation Université de Toulouse (2009) Toulouse.

[9] M. D. Ramdane, M. Hamel, Z. Dellil, A. Azzi, *Étude de l'influence de l'amplitude d'onde sur le transfert thermique et les pertes de charge dans un tube ondulé*, in: J.J. Bezina, R. Bennacer, M. El Hafi, A. Bounaceur, B. Ladevie, D. Lecomte, N. Lyczko (Eds.), 13$^{\text{èmes}}$ Journées Internationales de Thermique, France, 2007, pp. 1–5.

[10] D. Stanciu, M. Marinescu, A. Dobrovicescu, Etude comparative des irréversibilités dans la convection forcée le long d'une surface plane et ondulée (2008), https://www.agir.ro/buletine/581.pdf, Accessed 07 Jul 2025.

[11] E. Kim, *Natural convection along a wavy vertical plate to non-Newtonian fluids*, International Journal of Heat and Mass Transfer 40 (13) (1997) 3069–3078.

[12] S. Siddiqa, A. Hossain, *Natural convection flow over wavy horizontal surface*, Advances in Mechanical Engineering 2013 (5) (2013) Article ID 743034.

[13] L. S. Yao, *Natural convection along a vertical wavy surface*, ASME Journal of Heat Transfer 105 (3) (1983) 465–468.

[14] J. K. Lee, R. S. R. Gorla, S. Nakamura, I. Pop, *Mixed convection in wall plume of power-law fluids*, Acta Mechanica 102 (1994) 47–58.

[15] W. R. Risbeck, T. S. Chen, B. F. Armaly, *Laminar mixed convection over horizontal flat plates with power-law variation in surface temperature*, International Journal of Heat and Mass Transfer 36 (7) (1993) 1859–1866.

[16] P. P. Roy, S. Chowdhury, M. H. Raj, M. Q. Islam, S. Saha, *Forced, natural and mixed convection of non-Newtonian fluid flows in a square chamber with moving lid and discrete bottom heating*, Results in Engineering 17 (2023) Article ID 100939.

[17] N. Rehman, R. Mahmood, A.F. Majeed, I. Khan, A. Mohamed, *Multigrid simulations of non-Newtonian fluid flow and heat transfer in a ventilated square cavity with mixed convection and baffles*, Scientific Reports 14 (1) (2024) Article Number 6694.

[18] C. Mahboub, *Etude des phénomènes de transfert thermique dans les échangeurs de la chaleur destinés aux applications solaires*, Doctoral Dissertation Université Mohamed Khider Biskra (2011) Biskra.

[19] Z. K. Kadhim, H. O. Mery, *Influence of vibration on free convection heat transfer from sinusoidal surface*, International Journal of Computer Applications 136 (4) (2016).

[20] R. K. Ajeel, W. S. I. W. Salim, K. Hasnan, *Heat transfer enhancement in semicircle corrugated channel: Effect of geometrical parameters and nanofluid*, Journal of Advanced Research in Fluid Mechanics and Thermal Sciences 53 (1) (2019) 82–94.

[21] M. N. Hasan, S. C. Saha, Y. T. Gu, *Unsteady natural convection within a differentially heated enclosure of sinusoidal Corrugated Side Walls*, International Journal of Heat and Mass Transfer 55 (21–22) (2012) 5696–5708.

[22] E. Goncalves, *Implantation et validation de lois de paroi dans un code Navier-Stockes*, Doctoral Dissertation Ecole Nationale Supérieure de l'Aéronautique et de l'Espace (2001) France.

[23] N. Champagnat, *Différences finies et analyse numérique matricielle*, Master's Thesis Paris University (2010) France.

[24] A. Dimbiharizafy, I. A. Rakotozandry, J. A. Randriamorasata, *A two-dimensional numerical study of evaporation by mixed convection of an inclined damp flat plate: A lean engineering approach using DMADV methodology*, International Journal of Environment, Engineering and Education 7 (1) (2025) 71–83.

[25] G. Brillant, *Simulations des grandes échelles thermiques et expériences dans le cadre d'effusion anisotherme*, Doctoral Dissertation Institut National des Sciences Appliquées de Lyon (2004) France.

[26] H. Guittoun, *Étude numérique de transfert de chaleur convective mixte dans un canal à paroi inférieure ondulée*, Doctoral Dissertation Université Ibn Khaldoun de Tiaret (2010) Algeria.

[27] M. S. Abdallah, *tude de la convection naturelle thermique et massique laminaire et permanente dans la couche limite autour d'un tronc de cône à paroi sinusoïdale*, Doctoral Dissertation Université Mentouri Constantine (2006) Algeria.

[28] K. Doria, Viscosité: Introduction aux couches limites laminaires, Ecole Normale Supérieure Paris-Saclay, (2022),

https://eduscol.education.fr/sti/sites/eduscol.education.fr.sti/files/ressources/pedagogiques/14389/14389-viscosite-introduction-aux-couches-limites-laminaires-ensps.pdf, Accessed 07 July 2025.